



AFRL-OSR-VA-TR-2014-0241

**ON THE EVOLUTION FROM NON-PLASMONIC METAL NANOCCLUSERS TO PLASMONIC
NANOCRYSTALS**

**RONGCHAO JIN
CARNEGIE MELLON UNIVERSITY**

**09/24/2014
Final Report**

DISTRIBUTION A: Distribution approved for public release.

Air Force Research Laboratory
AF Office Of Scientific Research (AFOSR)/ RTE
Arlington, Virginia 22203
Air Force Materiel Command

REPORT DOCUMENTATION PAGE				<i>Form Approved</i> OMB No. 0704-0188	
Public reporting burden for this collection of information is estimated to average 1 hour per response, including the time for reviewing instructions, searching existing data sources, gathering and maintaining the data needed, and completing and reviewing this collection of information. Send comments regarding this burden estimate or any other aspect of this collection of information, including suggestions for reducing this burden to Department of Defense, Washington Headquarters Services, Directorate for Information Operations and Reports (0704-0188), 1215 Jefferson Davis Highway, Suite 1204, Arlington, VA 22202-4302. Respondents should be aware that notwithstanding any other provision of law, no person shall be subject to any penalty for failing to comply with a collection of information if it does not display a currently valid OMB control number. PLEASE DO NOT RETURN YOUR FORM TO THE ABOVE ADDRESS.					
1. REPORT DATE (DD-MM-YYYY)		2. REPORT TYPE		3. DATES COVERED (From - To)	
4. TITLE AND SUBTITLE				5a. CONTRACT NUMBER	
				5b. GRANT NUMBER	
				5c. PROGRAM ELEMENT NUMBER	
6. AUTHOR(S)				5d. PROJECT NUMBER	
				5e. TASK NUMBER	
				5f. WORK UNIT NUMBER	
7. PERFORMING ORGANIZATION NAME(S) AND ADDRESS(ES)				8. PERFORMING ORGANIZATION REPORT NUMBER	
9. SPONSORING / MONITORING AGENCY NAME(S) AND ADDRESS(ES)				10. SPONSOR/MONITOR'S ACRONYM(S)	
				11. SPONSOR/MONITOR'S REPORT NUMBER(S)	
12. DISTRIBUTION / AVAILABILITY STATEMENT					
13. SUPPLEMENTARY NOTES					
14. ABSTRACT					
15. SUBJECT TERMS					
16. SECURITY CLASSIFICATION OF:			17. LIMITATION OF ABSTRACT	18. NUMBER OF PAGES	19a. NAME OF RESPONSIBLE PERSON
a. REPORT	b. ABSTRACT	c. THIS PAGE			19b. TELEPHONE NUMBER (include area code)

Final report

Project: **On the evolution from non-plasmonic metal nanoclusters to plasmonic nanocrystals**
AFOSR grant number: **FA9550-11-1-0147**

PI: **Rongchao JIN**

(Carnegie Mellon University, Department of Chemistry, 4400 Fifth Ave, Pittsburgh, PA 15213;
Phone: 412-268-9448 (o), Fax: 412-268-1061, Email: rongchao@andrew.cmu.edu)

In this project, our central theme was to create atomically precise metal nanoclusters and understand their optical properties, electron dynamics, and catalytic reactivity through precise correlation with the atomic structures determined by X-ray crystallography. Metallic nanomaterials hold an important position in the development of new materials for producing storable fuels from sustainable inputs. Fundamental understanding of the structural, electronic and optical properties of such nanomaterials will benefit the design of high performance materials for AF applications. The AF funding in the past 3 years has enabled our group's significant research on metal nanocluster materials. Our group has established the leading position in the field of atomically precise metal nanoclusters. Under the AF funding, we have published 46 peer-reviewed papers, 2 book chapters, 1 patent application (joint with National Energy Technology Laboratory).

One of the important properties of metal nanoclusters is the quantum size effect. Gold nanoclusters with size of a few dozen atoms exhibit discrete electronic energy levels, as opposed to the continuous band of conduction electrons in the metallic state. Conventional gold nanoparticles with size above 5 nm are well known to exhibit the surface plasmon resonance (SPR)—which is a distinct feature of the *metallic-state* nanoparticles. In contrast, when the particle size is shrunk to ~ 2 nm (equivalently ~ 200 gold atoms) the plasmon resonance disappears and a size-dependent bandgap (or HOMO-LUMO gap) becomes distinct, in other words, ultrasmall metal nanoparticles become semiconducting. The properties of nanoclusters become very sensitive to an even small variation of particle size (e.g. a single-atom difference). Thus, a conventional level of synthetic control over particle size at nanometer precision (e.g. \pm a fraction of nm) is far from sufficient, instead, *atomic* level of control is critical for ultrasmall nanoparticles.

To synthesize *atomically precise* nanoclusters apparently poses huge challenges to chemists! We chose the thiolate-protected gold nanoclusters as a model system (referred to as $\text{Au}_n(\text{SR})_m$, where SR represents thiolate, n and m are the numbers of gold atoms and ligands, respectively). We have developed a new methodology for precisely controlling nanocluster size and structure through our intense work. In the nanocluster field, the “holy grail” is to solve the atomic structures of nanoclusters by X-ray crystallography. To pin down every atom in the nanocluster (i.e. the total structure of nanoclusters) is of critical importance in order to fully understand the electronic property evolution and surface catalytic reactivity. We have successfully obtained five crystal structures ($\text{Au}_{20}(\text{SR})_{16}$, $\text{Au}_{23}(\text{SR})_{16}$, $\text{Au}_{24}(\text{SR})_{20}$, $\text{Au}_{36}(\text{SR})_{24}$, $\text{Au}_{133}(\text{SR})_{52}$) and is a leading group in this effort. Below we shall highlight some major achievements.

The first observation of FCC structure in nanoclusters (work published in *Angew. Chem.* **2012 as a VIP paper**). Since the reports of the decahedral Au_{102} nanocluster (2007, Kornberg group) and the icosahedral Au_{25} nanocluster (2008, Jin and Murray groups) and the

biicosahedral Au_{38} nanocluster (2010, Jin group), researchers came to realize that the atomic structures of nanoclusters would be fundamentally different from the inherent face-centered cubic (FCC) structure of gold (both the bulk and nanoparticle forms). This raises a major question: Why is the FCC structure no longer favored in the nanoclusters? Is it simply a size effect or something else? We finally revealed this mystery with the attainment of the significant FCC structure of the super robust $\text{Au}_{36}(\text{SR})_{24}$ nanocluster. The key insight is the major role of the ligand. By choosing 4-*tert*-butylbenzenethiol (TBBT), we successfully coaxed out the FCC structure. The robust structure of $\text{Au}_{36}(\text{SR})_{24}$ exhibits a truncated tetrahedral shape and consists of an Au_{28} kernel exposing well-defined $\{100\}$ and $\{111\}$ facets (Fig 1). Unlike the previously reported $\text{Au}_n(\text{SR})_m$ nanocluster structures, a new type of thiolate binding mode was discovered, that is, the bridge-like binding of thiolate to the underlying Au atoms—which is for the first time observed in nanoclusters. The high stability of the nanocluster originates from the geometric structure and large bandgap (1.7 eV). The new FCC tetrahedral kernel and the thiolate bridging mode (as opposed to staple motifs) offer important implications for possible larger structures as well as for thiol binding on extended gold surfaces in self-assembled-monolayer (SAM) systems.

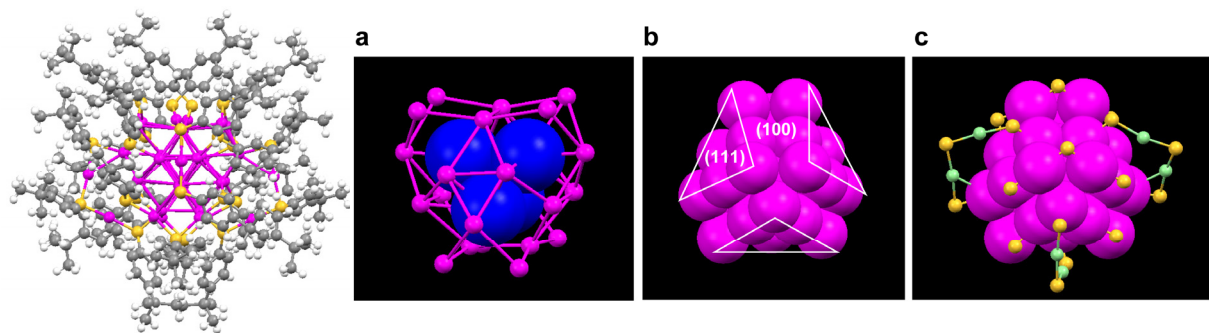


Figure 1. Total structure of $\text{Au}_{36}(\text{SPh-}^t\text{Bu})_{24}$ (left panel) and anatomy of the structure (right, a-c). **a)** Tetrahedral structure of the Au_{28} kernel, the inner Au_4 tetrahedron is shown in space-filled fashion, **b)** the two-shelled Au_{28} kernel exhibits bulk-like (111) and (100) faces, **c)** the surface protection of the Au_{28} tetrahedron by 4 dimeric staples and 12 bridging thiolates.

The hitherto largest-ever crystal structure $\text{Au}_{133}(\text{SR})_{52}$ solved (to be published). In our recent work, we have achieved the hitherto largest crystallographic structure — a chiral gold nanocluster possessing 133 gold atoms and 52 surface protecting thiolate ligands (Fig. 2). Remarkably, the $\text{Au}_{133}(\text{SR})_{52}$ nanocluster (where, $\text{R} = \text{SPh-}p\text{-Bu}^t$) exhibits aesthetic orderings in structure from the gold kernel to the Au-S interface to the carbon tails of thiols with a kaleidoscope of patterns at the atomic, molecular and ensemble scales: (i) the gold kernel follows a shell-by-shell growth pattern, forming a quasi-spherical Au_{107} kernel comprising a Au_{55} bi-shelled icosahedron and a third Au_{52} transition shell; (ii) The gold-thiolate interface exhibits a helical “stripe” pattern in which the S-Au-S motifs stack into ladders in the curved space (Fig. 3); (iii) The carbon tails of thiols further form “swirl” patterns independent of the underlying S-Au-S “stripe” patterns. The S-Au-S helical stripes provide the first crystallographic proof for the formation of self-assembled monolayer (SAM) structures on the curved surface of nanoparticles, and offer clues to the SAMs on flat surfaces. The -S-Au-S- helical stripes, together with carbon-tail swirls on the spherical gold kernel, also illustrate the unique patterning on the curved surface. These self-assembled hierarchical patterns in the chiral $\text{Au}_{133}(\text{SR})_{52}$ nanocluster has not been observed in the previously reported gold nanocluster structures—which are all smaller than $\text{Au}_{133}(\text{SR})_{52}$, implying that the size of $\text{Au}_{133}(\text{SR})_{52}$ is sufficiently large so as to manifest the

unprecedented pattern structures. The beautiful structure of $\text{Au}_{133}(\text{SR})_{52}$ reveals nature's patterning strategies in fabricating large and robust nanostructures.

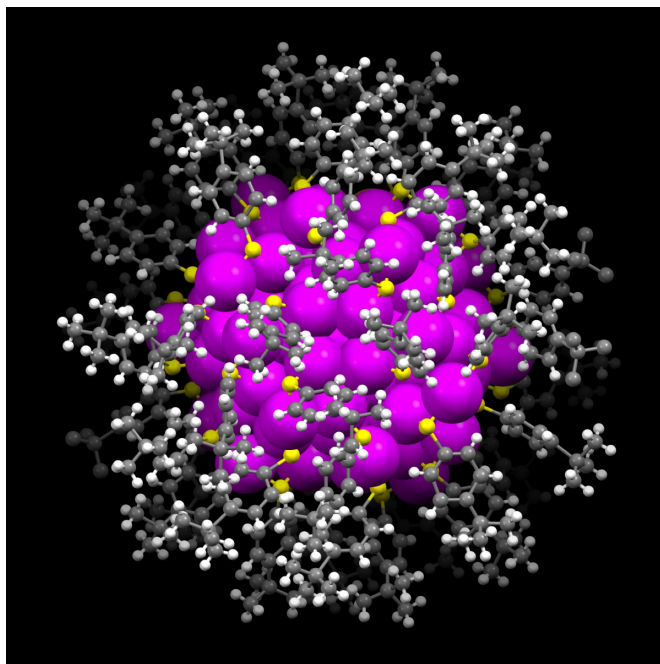


Figure 2. (A) Total structure of chiral $\text{Au}_{133}(\text{SR})_{52}$ determined by single crystal X-ray crystallography. Magenta: gold; yellow: sulfur; grey: carbon; white: hydrogen.

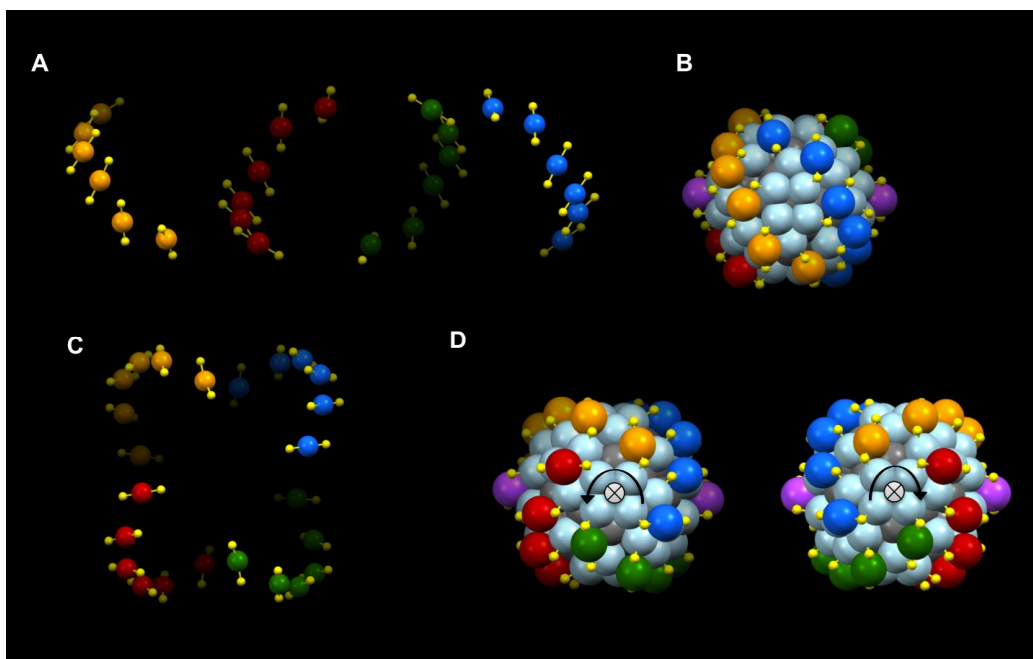


Figure 3. Self-assembled $-\text{S}-\text{Au}-\text{S}-$ helical stripes on the spherical Au_{107} kernel. (A,B) side views, and (C, D) top views; The two chiral isomers are shown in (D). Each stripe is composed of six monomeric staples stacked into a ladder-like helical structure. Yellow: sulfur; orange/red/blue/green: gold in the helices. Purple: gold in the independent monomeric staples.

Chiral nanoclusters (work published in *J. Am. Chem. Soc.* 2014). Chiral nanostructures have attracted wide interest in nanoscience research. We reported a new chiral structure in their recent work, i.e. the $\text{Au}_{20}(\text{SR})_{16}$ nanocluster (note: Au_{102} (Kornberg group) and Au_{38} (Jin group) were earlier reported to be chiral). Two isomers (i.e. left- and right-handed) are discovered (Fig 4). For each isomer, the kernel is composed of a bitetrahedral Au_7 . An unprecedented “ring” motif— $\text{Au}_8(\text{SR})_8$ was discovered. The ring protects the Au_7 kernel through strong $\text{Au}_{(\text{ring})}-\text{Au}_{(\text{kernel})}$ bonding but does not involve $\text{S}-\text{Au}_{(\text{kernel})}$ bonding, in contrast to the common “staple” motifs in which the $\text{S}-\text{Au}_{(\text{kernel})}$ bonding is dominant but the $\text{Au}_{(\text{staple})}-\text{Au}_{(\text{kernel})}$ interaction is weak (i.e. aurophilic). The chirality of the $\text{Au}_{20}(\text{SR})_{16}$ nanocluster arises from the peculiar arrangements of the octomeric ring and the trimeric and monomeric staples. As the smallest member in the TBBT (abbreviation of SPh-Bu^t) “magic series”, $\text{Au}_{20}(\text{TBBT})_{16}$ together with $\text{Au}_{28}(\text{TBBT})_{20}$, $\text{Au}_{36}(\text{TBBT})_{24}$ and $\text{Au}_{44}(\text{TBBT})_{28}$ reveals remarkable size-growth patterns in both geometric structure and electronic nature.

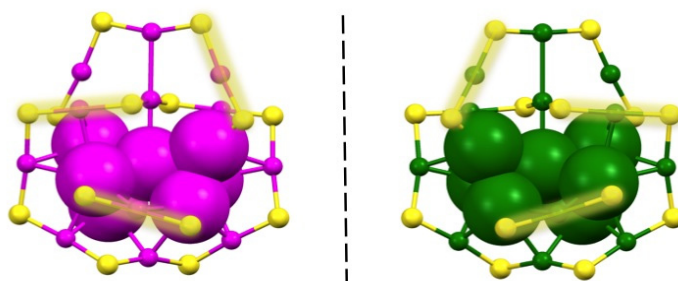


Figure 4. X-ray structure of chiral $\text{Au}_{20}(\text{TBBT})_{16}$ (where $\text{TBBT}=4\text{-tert-butylbenzenethiolate}$). Color codes: Magenta/ green: gold atoms in different enantiomers, Yellow: sulfur. The $\text{Ph-}t\text{-Bu}$ tails are omitted for clarity.

Single-atom level manipulation in nanoclusters (two papers published in *J. Am. Chem. Soc.* 2012, one was featured in *JACS Spotlights*). The heteroatom substitution in gold nanoclusters allows one to probe the atomic level sensitivity of the nanocluster’s optical and catalytic properties, as well as imparting the nanocluster with new properties, such as magnetic property. Gold-based bimetallic nanocluster catalysts often offer advantages resulting from the “synergy” of gold and a second metal. The atomically precise bimetallic nanoclusters will offer deep insight into the nature of the “synergy”. We succeeded in preparing a single-platinum-atom-doped gold nanocluster, $\text{Pt}_1\text{Au}_{25}(\text{SR})_{18}$ (Fig. 5), with the Pt atom uniquely located in the center of the cluster. Large perturbations to the electronic structure and optical properties were observed.

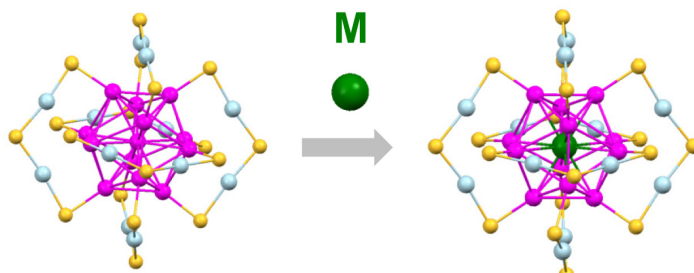


Figure 5. Single atom doping of gold nanocluster (e.g. $\text{Pt}_1\text{Au}_{24}(\text{SR})_{18}$).

In contrast with single-atom doping into a nanocluster, we also succeeded in dislodging a single Au atom out of the *rod-shaped* Au_{25} nanocluster protected by PPh_3/SR ligands (published

in *JACS* 2012). As shown in Fig. 6, the Au_{24} structure is a *non*-centered, bi-capped pentagonal prismatic Au_{12} core further capped by two pentagonal “hats” (Fig. 6). This *non*-centered pentagonal prismatic structural motif is unprecedented in gold cluster structures. The single-atom dislodging causes large changes to the optical spectrum of Au_{24} compared to the spectrum of Au_{25} nanoclusters (Fig. 7 a and b). In the case of Au_{25} , previous DFT calculations revealed that the 670 nm band was the HOMO-LUMO transition and is caused by the interactions between the two complete icosahedral Au_{13} units. We have carried out DFT calculations on the $[\text{Au}_{24}(\text{PPh}_3)_{10}(\text{SC}_2\text{H}_4\text{Ph})_5\text{X}_2]^+$ nanocluster, too. The lowest-energy peak at 560 nm was identified to arise from the HOMO-1 to LUMO+2 electronic transition (Fig. 7c, d).

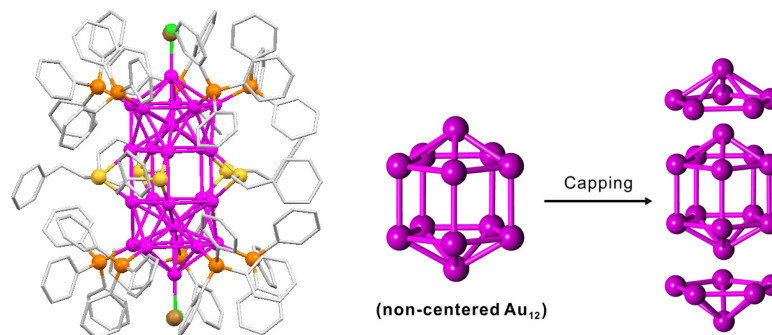


Figure 6. Dislodging a single atom out of $[\text{Au}_{25}(\text{PPh}_3)_{10}(\text{SC}_2\text{H}_4\text{Ph})_5\text{X}_2]^{2+}$ gives rise to $[\text{Au}_{24}(\text{PPh}_3)_{10}(\text{SC}_2\text{H}_4\text{Ph})_5\text{X}_2]^+$. Left: total structure. Middle: a non-centered Au_{12} unit; right: two Au_6 units.

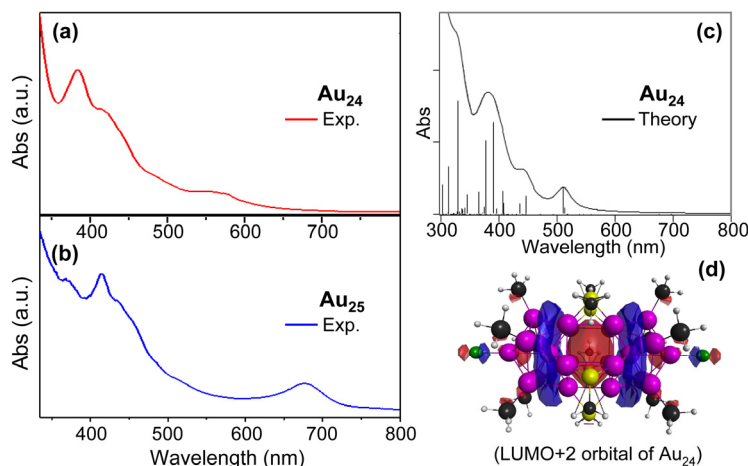


Figure 7. (a) Experimental optical spectrum of $[\text{Au}_{24}(\text{PPh}_3)_{10}(\text{SC}_2\text{H}_4\text{Ph})_5\text{X}_2]^+$ (in dichloromethane), (b) Experimental optical spectrum of $[\text{Au}_{25}]^{2+}$ (in dichloromethane), (c) DFT simulated optical spectrum of $[\text{Au}_{24}]^+$ model cluster, and (d) The LUMO+2 molecular orbital of $[\text{Au}_{24}]^+$.

Size-focusing methodology for precise control of nanoclusters with atomic precision.

Our work has established a successful, universal size-focusing methodology, which permits size-controlled synthesis of a series of $\text{Au}_n(\text{SR})_m$ nanoclusters, such as Au_{20} , Au_{23} , Au_{36} , Au_{55} , Au_{64} , and the largest-ever Au_{333} . Fig. 8 shows the example of $\text{Au}_{64}(\text{SC}_6\text{H}_{11})_{32}$. our methodology involves two key steps: a polydisperse $\text{Au}_n(\text{SR})_m$ mixture with an *appropriate* size distribution is first prepared via precise kinetic-control; then, these polydisperse nanoclusters are converged into *single-sized* nanoclusters by effecting size-focusing under proper conditions. The major principle underlying the size-focusing methodology is the different stability of different-sized

nanoclusters; the latter constitutes the basis for the selection of the most robust size by size-focusing under controlled conditions.

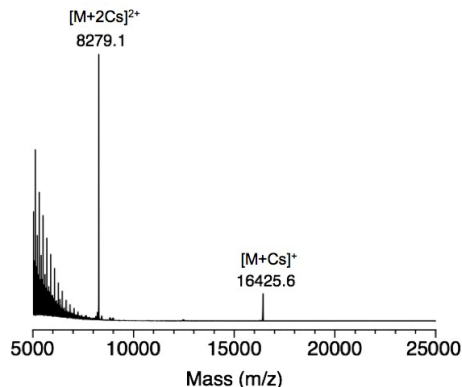


Figure 8. ESI mass spectrum of the $\text{Au}_{64}(\text{SC}_6\text{H}_{11})_{32}$ nanocluster. CsOAc was added to form Cs^+ adducts with the charge-neutral nanoclusters. The low m/z “comb” is due to $(\text{CsOAc})_n\text{Cs}^+$ peaks.

Optical properties of $\text{Au}_n(\text{SR})_m$ nanoclusters. In collaboration with Thomas group (Univ of Central Florida), we investigated the size-dependent nonlinear optical properties of semiconducting $\text{Au}_{25}(\text{SR})_{18}$, $\text{Au}_{38}(\text{SR})_{24}$, $\text{Au}_{144}(\text{SR})_{60}$ and metallic/plasmonic ~ 4 nm nanoparticles (work published in *Nano Lett.*). Our studies reveal remarkable features of the distinct evolution of the optical nonlinearity as the clusters progress in size from the *nonplasmonic* regime to the plasmonic regime. The smaller clusters (Au_{25} and Au_{38}) do not show saturable absorption at the surface plasmon wavelength of larger gold nanocrystals (Figure 9). Consequently, the third-order optical nonlinearity in these ultrasmall gold clusters exhibits a significantly lower threshold for optical power limiting. This limiting efficiency, which is superior to that of plasmonic nanocrystals, is highly beneficial for optical limiting applications.

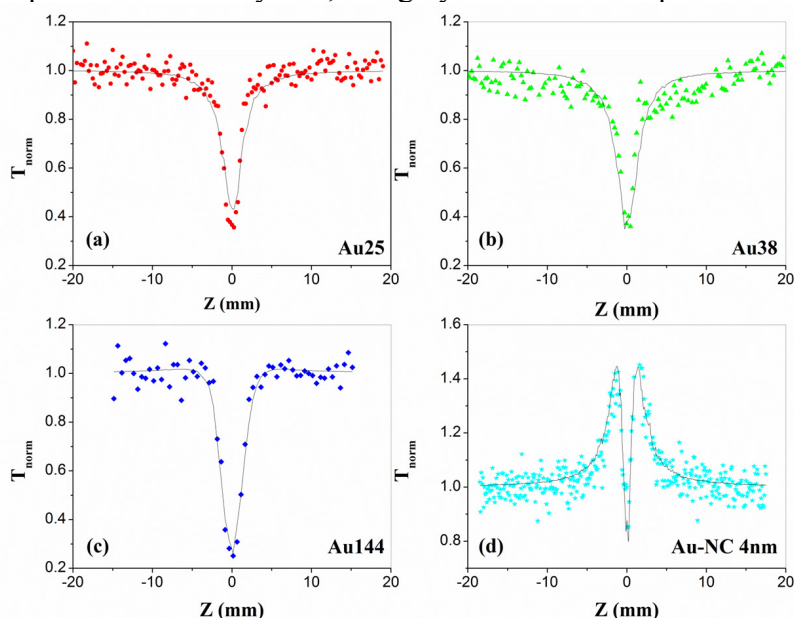


Figure 9. Open-aperture z-scans measured in the Au clusters and nanocrystals. (a) Au_{25} , (b) Au_{38} , (c) Au_{144} , and (d) Au nanocrystals (~ 4 nm). Samples are excited using 5 ns laser pulses at 532 nm. The valley shaped curves of Au_{25} and Au_{38} indicate pure optical limiting behavior, while the humps flanking the valley in Au_{144} signify the onset of saturable absorption. Absorption saturation is significant in the larger nanocrystals, as indicated by the strong peaks.

Electron dynamics of metal nanoclusters and probing the onset of metallic state. The relatively small $\text{Au}_n(\text{SR})_m$ nanoclusters (e.g. $n < 50$) possess quite large energy gaps (e.g. 1-3 eV). With increasing size, large nanoclusters (> 50 atoms) have diminishing band gap energies. Ultrafast spectroscopy has been used to probe the electron relaxation dynamics. In our recent work (to be published), we probed whether the $\text{Au}_{133}(\text{SR})_{52}$ nanoparticle is in the metallic state by performing state-state (Fig. 10).

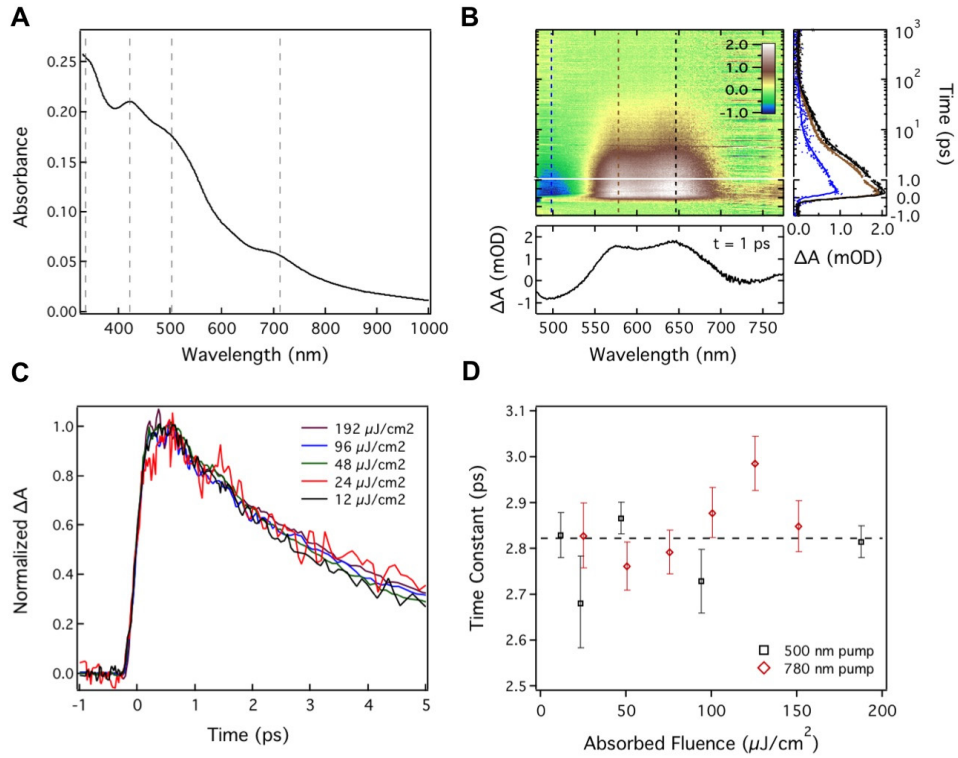


Figure 10. (A) Linear extinction spectrum of $\text{Au}_{133}(\text{SR})_{52}$ nanoparticles in toluene. The dashed lines represent peak positions extracted from fitting to a series of inhomogeneously broadened transitions and a non-resonant scatter background. (B) Image plot of transient absorption data with optical pumping at 420 nm, along with representative kinetics at wavelengths corresponding to the dashed lines in the image plot (right panel) and transient spectra (bottom panel) at 1 ps. (C) Normalized decay kinetics as a function of laser fluence with 500 nm pump pulses and (D) extracted values of the rate constant for the faster decay component of a two-exponential fit showing the fluence independence of the carrier dynamics.

UV-vis absorption and femtosecond-transient optical measurements. The $\text{Au}_{133}(\text{SR})_{52}$ nanoparticles exhibit a highly structured UV-vis spectrum with absorption bands at 336 nm, 421 nm, 503 nm, and 712 nm (Fig. 10A), being distinctly different from the single plasmon band (e.g. at ~ 520 nm) of metallic-state spherical nanoparticles. Thus, $\text{Au}_{133}(\text{SR})_{52}$ nanoparticles are nonmetallic in nature, which is further supported femtosecond broadband transient absorption measurements. Upon photoexcitation above the optical gap, we observe three primary transient optical features (Fig. 10B), including a net bleach near 500 nm and two net positive features of excited state absorption at ~ 580 and 640 nm (Fig. 10B lower panel). The bleach at 500 nm correlates to the ground state transition at 503 nm observed in Fig. 10A. The other ground state transition observed at 712 nm is superimposed on the excited state absorption features such that

no net negative signal can be seen. These overlapping contributions cannot be rigorously separated (using global analysis, for example) since identical kinetics are observed at all wavelengths in our data set. This is illustrated in the right panel of Fig. 10B, where decay kinetics at each of the three primary transient features can globally fit with just two time constants (~ 2.8 ps and ~ 30 ps). The absence of more complex spectral dynamics suggests that a single electronic configuration is responsible for all of the resolvable transient features. This is in contrast with the expected dynamics for a metallic-state nanoparticle. Most importantly, all of the observed relaxation dynamics are independent of laser fluence, in sharp contrast to metallic noble metal nanoparticles. Normalized kinetic traces measured at either the bleach (500 nm) or the excited state absorption features (580 nm, Fig. 10C) can be superimposed over an absorbed fluence range of 12 – 192 $\mu\text{J}/\text{cm}^2$. Both the faster (~ 2.8 ps) and slower components (~ 30 ps) of the biexponential decay are found to be independent of pump fluence and pump wavelength (Fig. 10D).

These results significantly differ from the traditional carrier relaxation processes in metallic-state nanoparticles, where carrier cooling is described by the two-temperature model. Within this model, the rate of thermal equilibration between the electronic and lattice subsystems is described by a constant electron-phonon coupling term, such that an increase of the electronic temperature (at high laser fluence) results in a longer relaxation time. Taken together, our results suggest that despite its relatively large size, the unique structure of the $\text{Au}_{133}(\text{SR})_{52}$ nanoparticle delays the onset of metallic behavior.

Catalysis by Nanoclusters (two papers published in *JACS* 2012). Atomically precise metal nanoclusters provide exciting opportunities for catalysis research, such as the tuning of catalytic activity/selectivity at the single-atom level through controlled doping of nanoclusters, the study of structure-reactivity relationships of nanoclusters in solution or supported on solids, as well as the identification of catalytic sites at the atomic level. The crystallographic characterization reveals the atomic structure of nanoclusters, which permits identification of molecular adsorption geometry and elementary steps of catalytic reaction through combined experiment and theory. Such information is important for fundamental understanding of catalytic processes and rational design of catalysts. Gold was once thought to be catalytically inert, but research since the late 1980s has demonstrated its excellent catalytic properties. A key to achieving high catalytic performance is the small particle size (<3 nm preferred), as well as precise control of the surface atomic structure since catalysis is essentially about the surface. Larger Au nanoparticles are metallic and exhibit surface plasmon properties that hold promise in optical and biomedical applications, but are generally not active in catalysis. We discovered that thiolated $\text{Au}_n(\text{SR})_m$ nanoparticles are indeed excellent catalysts for some reactions.

In regard to the applications in energy storage and utilization, recent exploration of gold nanoclusters (collaborative work with Matranga group at NETL) discovered that $\text{Au}_{25}(\text{SC}_2\text{H}_4\text{Ph})_{18}$ nanoclusters drastically reduce the undesired overpotential in the CO_2 reduction reaction down to merely 90 mV of the formal potential (i.e. thermodynamic limit), representing a ~ 300 mV improvement over larger Au nanoparticles and bulk Au (Fig. 11). Peak CO_2 conversion occurred at -1V (vs. RHE) with $\sim 100\%$ efficiency and a rate $\sim 7\text{--}700$ times higher than larger Au catalysts and $\sim 10\text{--}100$ times higher than current state-of-the-art processes. DFT modeling indicates the above noted changes stem from a CO_2 -induced redistribution of charge within the cluster. The ultrasmall size of nanoclusters (dozens of metal atoms) offers extremely high atom-efficiency and thus greatly reduces the catalyst amount required in

electrocatalysis, unlike the commercial 20% Pt/C catalyst in which the high loading of Pt precludes wide application in fuel cells.

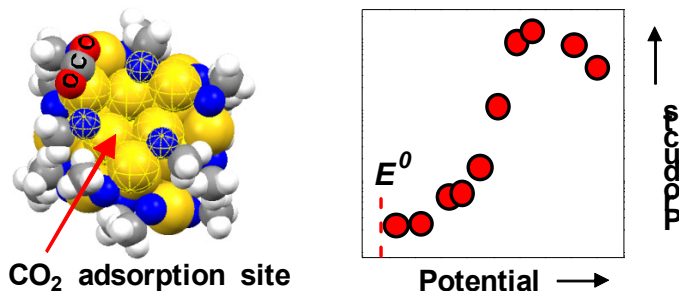


Figure 11. Electoreduction of CO₂ Catalyzed by Au₂₅(SR)₁₈ nanoclusters. The left figure shows the CO₂ adsorption site on the nanocluster simulated by DFT.

We also investigated the catalytic activity of the Pt₁Au₂₄ bimetallic cluster supported on TiO₂ for the selective oxidation of styrene with PhI(OAc)₂ as the oxidant (*JACS* 2012). Under mild conditions (at 70 °C), the PtAu₂₄(SR)₁₈/TiO₂ gave rise to 90.8% conversion of styrene, which is much higher than that of homogold Au₂₅(SR)₁₈/TiO₂ catalyst (~58.9% only), and the selectivity for the product benzaldehyde (89.9%) is also significantly higher than that of Au₂₅(SR)₁₈/TiO₂ catalyst (54.0%). These results show that the PtAu₂₄(SR)₁₈/TiO₂ catalyst has a remarkable enhancement in the catalytic activity/selectivity for styrene oxidation than the undoped Au₂₅(SR)₁₈/TiO₂ catalyst. The tunable characteristic of bimetallic nanoclusters will enable improvements in the catalytic activity, selectivity, and stability for specific reaction processes in both chemical and electrochemical catalysis.

In summary, this research program focused on novel atomically precise Au_n(SR)_m nanoclusters (SR=thiolate) in the size range from a dozen to several hundred gold atoms (equivalently 1-3 nm). These unique nanoclusters have been crystallographically characterized by single-crystal X-ray crystallography. We have investigated the molecular-like properties of nanoclusters and evolution to the plasmonic properties with increasing size. Based upon the determined structures (atom-packing of the metal core and ligands), the electronic and optical properties are understood and correlated with the structures. We also investigate the catalytic application of Au_n(SR)_m nanoclusters. Such nanomaterials serve as the foundation for addressing the fundamental questions in the areas of efficient storage and utilization of light and chemical energy.